VTaNbAl: A class of spin gapless semiconductors with topological nontrivial features

Deepika Rani,[1,2,*] P. C. Sreeparvathy,[1,*] K. G. Suresh,[1] Ratnamala Chatterjee,[2,†] and Aftab Alam[1,‡]
[1]*Department of Physics, Indian Institute of Technology Bombay, Mumbai 400076, Maharashtra, India*
[2]*Department of Physics, Indian Institute of Technology Delhi, Hauz Khas, New Delhi 110016, India*

(Received 5 November 2022; revised 1 March 2023; accepted 4 April 2023; published 26 April 2023)

We report a class of spin gapless semiconductors (SGSs) hosting topological nontrivial features along with a fully compensated ferrimagnetic behavior in VTaNbAl, a quaternary Heusler alloy. Unlike conventional SGSs, this class of compounds acquires a unique band structure with opposite spin characters in the valence and conduction band edges, making them potential candidates for spin valves and a large anomalous Nernst effect. Interestingly, despite compensated ferrimagnetic (CF) behavior, VTaNbAl shows a reasonably large anomalous Hall effect possibly arising from the intrinsic nonvanishing Berry curvature. The CF state breaks the time-reversal symmetry and hence opens the possibility of Weyl nodes. We found four pairs of Weyl nodes located near the Fermi level leading to the nonvanishing Berry curvature, and hence a large anomalous Hall conductivity ($\sim$100 Ω^{-1} cm^{-1}). Our experimental synthesis confirms VTaNbAl to crystallize in a cubic Heusler structure with $A2$-type disorder. A magnetization measurement shows a very small saturation moment ($\sim 10^{-3}\mu_B$/f.u.), which agrees fairly well with our theoretical findings of fully compensated ferrimagnetism in the alloy. Resistivity shows a metalliclike nature, with the signature of disorder-induced weak localization in the low-temperature limit. The overall variation with varying temperature, however, is extremely weak.

DOI: 10.1103/PhysRevB.107.134434

I. INTRODUCTION

Spintronics has emerged as one of the most important topics of research in the field of magnetic materials today. The main role of these materials is to provide spin-polarized charge carriers, or spin currents. A major breakthrough along these lines occurred via the discovery of so-called spin gapless semiconductors (SGSs). Unlike conventional semiconductors or half-metallic ferromagnets, SGSs acquire a unique spin-resolved band structure with a finite band gap in one spin channel and a close (zero) gap for the other and thus are useful for tunable spin transport applications [1]. They are one of the latest classes of materials considered for spintronic devices. A few of the several advantages of SGSs include (i) a minimal amount of energy required to excite electrons from the valence to conduction band due to zero gap, (ii) the availability of both charge carriers, i.e., electrons as well as holes, which can be 100% spin polarized simultaneously, and (iii) easy separation of fully spin-polarized electrons and holes using the Hall effect. Bulk Co-doped $PbPdO_2$ was the first SGS reported using first-principles calculations [1]. This was followed by numerous reports on *ab initio* simulations predicting the SGS nature in different Heusler alloy systems [2–5].

In general, SGSs can be categorized into four different classes depending on how various conduction and valence bands corresponding to two different spin channels touch the Fermi level (E_F) [6]. Figure 1 shows the schematics of these four SGS classes. In "class A," the valence band maximum (VBM) and conduction band minimum (CBM) arise from the same spin channel, while there is a gap in the opposite spin channel [see Fig. 1(a)]. This corresponds to the conventional SGS, as mentioned before, and is reported ubiquitously in the literature. In "class B," the VBM and CBM arise from opposite spin channels [see Fig. 1(b)]. In this case, there is a gap between the conduction and valence bands for both the majority and minority spin channels, but there is no gap between the majority electrons in the VB and the minority electrons in the CB. In "class C" ("class D"), the VBM (CBM) arise only from one spin character while the CBMs (VBMs) arise from both spin channels. In other words, in class C, one spin channel is gapless while the other one is gapped with the VBM level lying below E_F and CBM touching E_F [see Fig. 1(c)]. On the other hand, in class D, one spin channel is gapless while the VBM level of the other spin channel touches E_F, which is separated from its corresponding CBM by a gap [see Fig. 1(d)].

Despite the potential of SGSs to attain 100% spin polarization, they typically produce large magnetic dipole fields that hinder the performance of spintronic devices that contain them [7]. Thus, materials that display 100% spin polarization but with very low or negligibly small net magnetic moment are highly desired. The fully compensated ferrimagnetic (FCF) materials usually contain three or more magnetic ions with their moments aligned in such a way that the net magnetization is zero or vanishingly small. There are many materials which are predicted to be FCF based on theoretical simulations such as MnCrSb [8], Cr_2CoGa [9], Cr_2MnZ (Z = P, As, Sb, Bi) [10], CrVXAl (X = Ti, Zr, Hf)

*These authors contributed equally to this work.
†ratnamalac@gmail.com
‡aftab@iitb.ac.in

 ©2023 American Physical Society

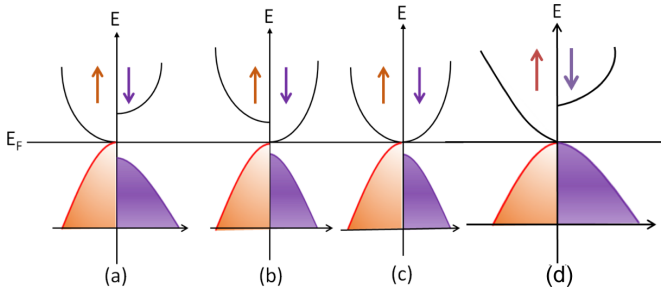

FIG. 1. Schematic energy band diagrams of four classes of spin gapless semiconductors (SGSs) with parabolic dispersion: (a) class A, (b) class B, (c) class C, and (d) class D.

[11], Mn_2Z (Z = Si, Ge) [12], and Mn_3Ga [13]. Recently, Venkateswara *et al.* [14] reported a fully compensated ferrimagnetic SGS nature in a CrVTiAl Heusler alloy. Heusler alloys are also well studied for various topological nontrivial properties [15,16]. Among them, magnetic systems are exemplified to be promising for hosting topological Weyl nodes due to the broken time-reversal symmetry [17,18]. A natural consequence of the Weyl nodes is the occurrence of nonzero Berry curvature which opens up the possibility of interesting anomalous transport properties in the system. The coexistence of magnetic and topological features in a material provides a fertile platform for potential spintronics applications [19,20]. There exist a few spintronic materials such as ferromagnetic, half-metallic, spin-gapless semiconductors, etc., which are reported to also show potential topological nontrivial features [21,22]. A recent study of a compensated ferrimagnetic compound Ti_2MnAl showed a large anomalous Hall conductivity [23]. Yet, compared to other magnetic systems, compensated ferrimagnetic materials are less explored for their topological nontrivial features.

Here, we report a combined theoretical and experimental study of a composite quantum material, VTaNbAl, which shows three coexisting complimentary properties: (1) fully compensated ferrimagnetism, (2) class B SGS, and (3) four pairs of topological Weyl nodes near E_F. Our *ab initio* simulation confirms that there exists another energetically competing configuration (class A SGS with FCF), which hints towards the possibility of substitutional disorder at finite temperatures (T). Interestingly, this system also hosts four pairs of topological Weyl nodes near E_F, leading to a nonvanishing Berry curvature. This is mediated by the time-reversal symmetry breaking arising out of the FCF state. The simulated anomalous Hall conductivity is found to be reasonably high ($\sim$100 Ω^{-1} cm^{-1}) possibly arising from the topological nontrivial features of VTaNbAl. The room-temperature x-ray diffraction (XRD) data confirm a cubic Heusler structure with an $A2$-type structure. A magnetization measurement shows a very small saturation moment ($\sim 10^{-3}\mu_B$/f.u.), indicating the fully compensated ferrimagnetism in the alloy, as also confirmed by our *ab initio* simulation. Measured resistivity shows a weak T dependence with metalliclike behavior.

II. COMPUTATIONAL AND EXPERIMENTAL DETAILS

First-principles calculations are done using the Vienna *ab initio* simulation package (VASP) [24,25]. Other computational details are provided in the Supplemental Material (SM) [26] (see also Refs. [27–33] therein). A polycrystalline sample of VTaNbAl was prepared using the arc melting procedure. The polycrystalline alloy VTaNbAl was prepared by arc melting stoichiometric amounts of high-purity (at least 99.9% purity) constituent elements in an argon atmosphere. To further reduce the contamination, a Ti ingot was used as an oxygen getter. The ingots formed were flipped and melted several times for better homogeneity. Room-temperature x-ray diffraction patterns were taken using Cu $K\alpha$ radiation with the help of a Panalytic X-pert diffractometer. A phase purity and crystal structure analysis was done using the FULLPROF suite. Magnetization measurements were done using a vibrating sample magnetometer (VSM) attached to a physical property measurement system (PPMS) (Quantum Design) for fields up to 70 kOe. Electrical resistivity and Hall measurements were measured in a cryogen-free measurement system from Cryogenic Limited, U.K.

TABLE I. For VTaNbAl, theoretically optimized lattice parameter (a_0), total and atom-projected moments (μ_B), and relative total energy (ΔE) of type I, II, and III ordered configurations using the GGA+U approximation.

Type	a_0 (Å)	m^{Nb}	m^{V}	m^{Ta}	m^{Total}	ΔE (meV/atom)
I	6.60	−0.87	+3.01	−2.14	0.0	0
II	6.61	−1.00	+2.55	+0.77	2.32	210
III	6.62	−1.75	+3.03	−1.20	0.08	9

VTaNbAl belongs to a quaternary Heusler alloy with a LiMgPdSn prototype structure (space group $F\bar{4}3m$). The structure can be visualized as four interpenetrating fcc sublattices with Wyckoff positions 4a, 4b, 4c, and 4d. In general, for a quaternary $XX'YZ$ alloy, there exist three energetically nondegenerate configurations (keeping Z at the 4a site). They are (type I) X at 4c, X' at 4d, and Y at 4b sites, (type II) X at 4b, X' at 4d, and Y at 4c sites, and (type III) X at 4c, X' at 4b, and Y at 4d. The crystal structures of these three configurations for VTaNbAl along with the corresponding Brillouin zone are presented in Fig. S1 of SM [26].

III. THEORETICAL RESULTS

Table I shows the optimized lattice parameters, atom-projected and total moments, and relative energies (ΔE) of type I, II, and II configurations of VTaNbAl using the generalized gradient approximation (GGA+U) functional [34]. The Hubbard U values for Nb, V, and Ta are 1.55, 5.61 and 3.66 eV, which are calculated self-consistently (see SM [26] for further details about this calculation). Clearly, type I and III configurations exhibit an almost fully compensated ferrimagnetic nature, whereas type II has a total moment of 2.30μ_B. In the type I and III configurations, V is antiparallel to Nb and Ta, whereas in the type II configuration, Nb is antiparallel to V and Ta. Interestingly, the energy difference between type I and III configurations is very small (9 meV/atom), indicating the possibility of disorder. Figure 2 shows the spin-polarized band structure and density of states (DOS) for three configurations of VTaNbAl. The atom-projected DOS and band structures for these three configurations are shown in SM

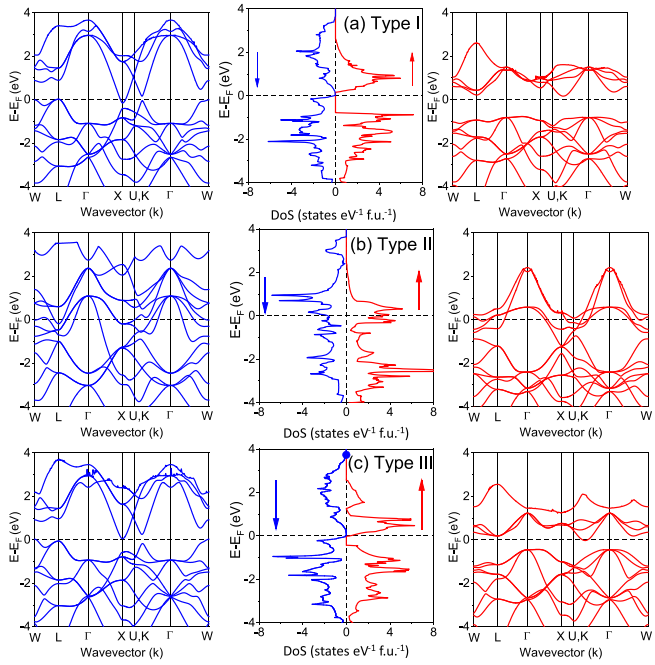

FIG. 2. Spin-resolved band structure and density of states (DOS) for (a) type I, (b) type II, and (c) type III configurations of VTaNbAl using the GGA+U approximation.

[26]. Type I and III configurations confirm the class A and B nature of SGS, respectively, while type II is metallic. This can be confirmed from a combined majority and minority band structure (and density of states) plot, as shown in Figs. S3 and S4 of SM [26]. Notice that, for a type III configuration, the VBM and CBM have opposite spin characters and touch each other directly at E_F, a prerequisite for a class B SGS.

Among the theoretically predicted materials, another example of a class B SGS is FeVHfSi [35], which was found to have a similar band structure, as observed for VTaNbAl. Gao *et al.* [35] proposed that among the different types of SGSs, class B SGSs hold special importance because in these types of materials, the VBM and CBM have different spin characters, and thus the spin polarization of the longitudinal resistivity can be easily tuned by controlling the chemical potential. This makes them potential candidates for fabricating spin valves which are suitable for electrostatic gating. In addition to this, the spin character of the carriers changes when they are excited from VBM to CBM, which results in the sign change of anomalous Hall conductivity across E_F, corresponding to a large anomalous Nernst effect. Thus, class B SGSs are promising candidates for fabricating spintronic field-effect transistors.

Next, we present the topological nontrivial features of VTaNbAl in its lowest-energy structural configuration (i.e., type I). This is the only configuration which exhibits topological nontrivial features, as explained below. It is to be noted that compensated ferrimagnetism breaks time-reversal symmetry, which opens up the possibility of Weyl-type band crossings. The search for nodal points in the entire Brillouin zone reveals the existence of four pairs of Weyl nodes with chirality ± 1 for a type I configuration near the Fermi level.

TABLE II. For a type I configuration of VTaNbAl, the coordinates of four pairs of Weyl points in direct coordinates.

Coordinates of Weyl points	Chirality
$\overline{W}_1(-0.03, 0.29, -0.31)$	$+1$
$\overline{W}_2(0.04, 0.32, -0.28)$	-1
$\overline{W}_3(0.60, 0.28, 0.32)$	$+1$
$\overline{W}_4(0.60, 0.32, 0.27)$	-1
$\overline{W}_5(-0.32, -0.05, 0.27)$	$+1$
$\overline{W}_6(-0.28, 0.03, 0.32)$	-1
$\overline{W}_7(-0.32, -0.59, -0.27)$	$+1$
$\overline{W}_8(-0.28, -0.60, -0.32)$	-1

These chirality values indicate the source and sink nature of the Berry curvature. The locations of these Weyl points and their chirality values are listed in Table II. The total chirality value involving all the Weyl points vanishes, as expected [36]. A three-dimensional visualization of the location of these eight Weyl points is displayed in Fig. 3(a). Red and blue colored spheres represent the Weyl points with $+1$ and -1 chirality, respectively. Figure 3(b) shows the bulk band dispersion around one such Weyl mode ($\overline{W}_1$ from Table II), exhibiting a linear dispersion indicating the type I nature of the Weyl point. Notably, all the Weyl nodes are located above the Fermi level. The presence of multiple Weyl nodes cause a nonzero intrinsic Berry curvature. Figure 3(c) shows the Berry curvature in the k_x-k_y plane for a type I configuration of VTaNbAl. Both negative and positive high-intensity Berry flux is clearly evident from the figure. Surface states are one of the important features of a topological material. The four pairs of Weyl points are expected to acquire topologically protected surface states near the Fermi level (E_F). To better understand

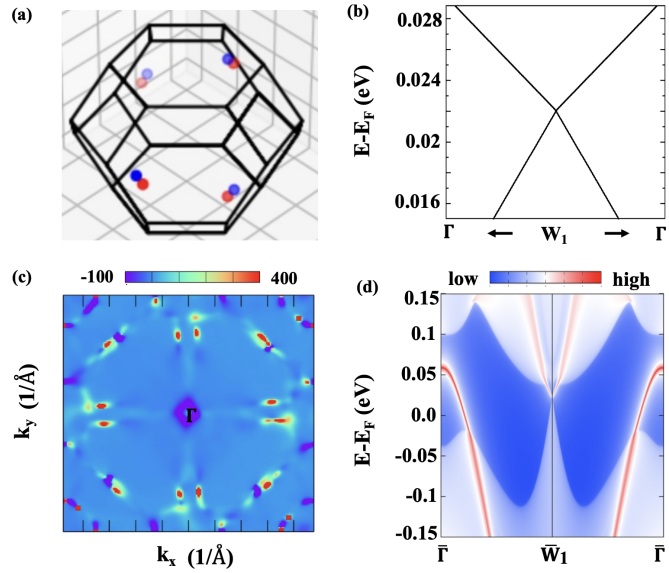

FIG. 3. For a type I configuration of VTaNbAl, (a) the location of four pairs of Weyl points in the three-dimensional (3D) BZ, (b) electronic band dispersion around one of the Weyl points ($\overline{W}_1$), (c) Berry curvature in the k_x-k_y plane, and (d) surface spectra around one of the Weyl points ($\overline{W}_1$) projected on a (001) surface.

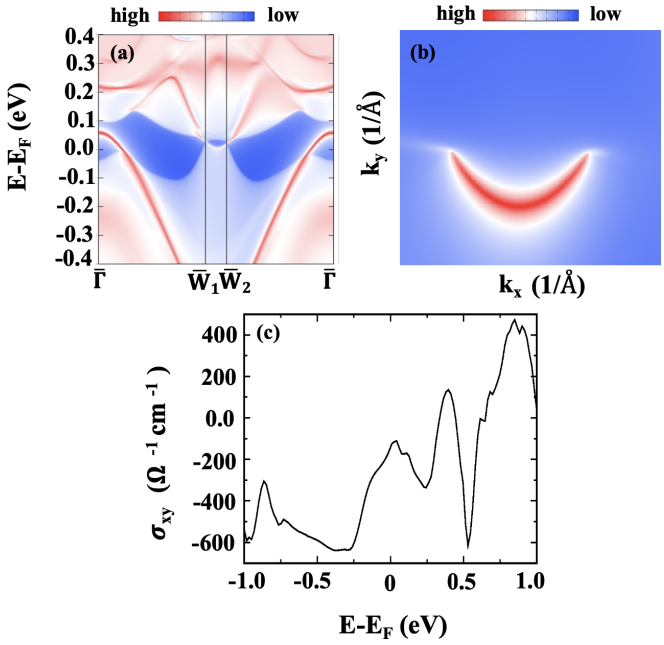

FIG. 4. For a type 1 configuration of VTaNbAl, (a) (001) surface spectra around two of the Weyl points ($\overline{W}_1$ and $\overline{W}_2$), (b) Fermi arc on the k_y-k_z plane originated from the Weyl points ($\overline{W}_1$ and $\overline{W}_2$), and (c) energy-dependent anomalous Hall conductivity (σ_{xy}).

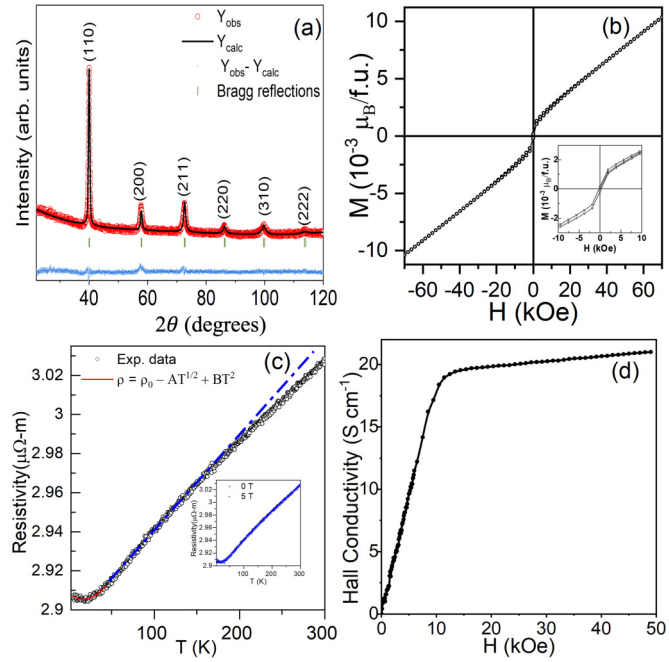

FIG. 5. For VTaNbAl, (a) room-temperature XRD and Rietveld refined data. (b) Magnetization (M) vs field (H) at 5 K. The inset shows a zoomed-in view. (c) Resistivity (ρ) vs T along with the low and high T fitting in zero field. The dashed blue line indicates the linear trend expected for electron-phonon scattering. The inset shows ρ vs T in 0 and 50 kOe. (d) Hall conductivity (σ_{xy}) vs H at 5 K.

the nature of these states, we have first simulated the surface states concentrated around one of the Weyl points ($\overline{W}_1$) by projecting it on a (001) surface [see Fig. 3(d)]. It clearly shows a highly linearized surface state near E_F, yet with a bit of reduced visibility possibly due to the prominent contribution of bulk states at/near E_F. Next, we selected two adjacent Weyl points with opposite chiralities ($\overline{W}_1$ and $\overline{W}_2$ from Table II), and projected them on a (001) surface. The simulated surface states connect these two Weyl points as shown in Fig. 4(a). They have a similar feature as Fig. 3(d), but illustrate how the surface contributions at the two Weyl points are connected with each other. Further, we have calculated the surface arc originating due to these Weyl points, as shown in Fig. 4(b). The Berry curvature is then integrated over the entire Brillouin zone (BZ) to simulate the anomalous Hall conductivity (AHC) [37]. Figure 4(c) shows the energy dependence of AHC, with a maximum value of 600 Ω^{-1} cm^{-1} at/around $\pm$0.5 eV away from E_F. The AHC value at E_F is also reasonably high, i.e., 100 Ω^{-1} cm^{-1}. Such a high value is comparable with those reported for other ferromagnetic and compensated ferrimagnetic materials, e.g., Ti_2MnAl [23].

IV. EXPERIMENTAL RESULTS

A. Crystal structure

For a quaternary Heusler alloy $XX'YZ$ (crystallizing in a Y-type structure), the structure factor of a type I configuration is

$$F_{hkl} = 4\left(f_Z + f_Y e^{\pi i(h+k+l)} + f_X e^{\frac{\pi}{2}i(h+k+l)} + f_{X'} e^{\frac{-\pi}{2}i(h+k+l)}\right), \quad (1)$$

where f_X, $f_{X'}$, f_Y, and f_Z are the atomic scattering factors of X, X', Y, and Z elements, respectively. For superlattice reflections (111) and (200), F_{hkl} can be written as

$$F_{111} = 4[(f_Y - f_Z) - i(f_X - f_{X'})], \quad (2)$$

$$F_{200} = 4[(f_Y + f_Z) - (f_X - f_{X'})]. \quad (3)$$

Intensities of the fcc (111) and (200) peaks play a crucial role in dictating the ordered versus disordered phase of the material. The system will be ordered if both peaks are present, $B2$ disordered (where Y and Z and X and X' atoms are randomly distributed) if only the (200) peak is present, and $A2$-type completely disordered if both peaks are absent. All positions become equivalent in the $A2$ (tungsten-type) structure with a bcc lattice and reduced symmetry ($Im\bar{3}m$). Figure 5(a) shows the Rietveld refined x-ray diffraction (XRD) pattern of VTaNbAl at room temperature considering the $A2$-type structure ($Im\bar{3}m$) where all four atoms occupy the four Wyckoff positions with equal probability. The absence of both (111) and (200) superlattice reflection peaks in the present case indicates the possibility of $A2$ disorder. The measured cubic lattice parameter is found to be 3.22 Å, with a χ^2 value of 2.03. In Heusler alloys, the chemical nature of the constituent elements strongly dictates the type of structural ordering. The least electronegative element has the tendency to occupy octahedral sites [38], while, if they have similar electronegativities, they compete to occupy the same site, which leads to the disorder. The nearly similar electronegativities of Nb, V, Ta, and Al (1.60, 1.63, 1.50, and 1.61, respectively) strongly suggest the

possibility of *A*2-type disorder in VTaNbAl, which makes all four sites equally probable to be occupied by the four atoms.

B. Magnetic properties

Figure 5(b) shows the magnetization (M) versus field (H) at 5 K for VTaNbAl. In a completely ordered quaternary Heusler alloy, the saturation magnetization follows the Slater-Pauling (SP) rule [39], $M_s = N_v - 18$, where N_v is the total number of valence electrons. For VTaNbAl, N_v is 18 and hence M is expected to be zero. Figure 5(b) shows a negligibly small saturation magnetization ($\sim 10^{-3}\mu_B$/f.u.), confirming the FCF nature of this alloy. The thermomagnetic (M vs T) curve [in the zero-field-cooled (ZFC) and field-cooled (FC) mode] at $H = 500$ Oe is shown in Fig. S5 of SM [26], which confirms a high magnetic ordering temperature (>300 K) for VTaNbAl.

C. Transport properties

Figure 5(c) shows the resistivity (ρ) vs T data for VTaNbAl at 0 kOe. The inset shows the same plot at two different fields (0 and 50 kOe), confirming a weak field dependence and hence a negligibly small magnetoresistance value. In the low-T range ($T < 50$ K), ρ first decreases with increasing T, followed by a clear upturn. This feature may be attributed to the disorder-induced weak localization effect [40,41], which usually shows a $T^{1/2}$ dependence in the ρ expression. A similar behavior has been observed in several Heusler alloys and is attributed to the disorder present in the system [40]. In the low T regime (5 K $< T <$ 50 K), the data fit well with the following equation, $\rho(T) = \rho_0 + \rho(T) = \rho_0 - AT^{1/2} + BT^2$, where the T^2 term corresponds to one-magnon or electron-electron scattering. The dominant contribution however arises from the $T^{1/2}$ term. The values of ρ_0, A, and B were found to be 2.91 μΩ cm, 0.0016(2) μΩ cm K$^{-1/2}$, and 6.5(4) $\times 10^{-6}$ μΩ cm K^{-2}, respectively. For $T > 50$ K, the ρ vs T curve reflects a metalliclike behavior up to $T \sim 175$ K, above which it deviates from the linear behavior. A similar sublinear resistivity behavior has also been observed in other Heusler-based SGSs, such as CrVTiAl [42], and Mn_2CoAl films [43], and was attributed to an increase in the number of carriers with increasing temperature. In other words, for $T < 175$ K, the carrier density is constant and the resistivity is dominated by electron-phonon scattering, whereas for $T > 175$ K, the carriers become thermally activated.

Figure 5(d) shows the variation of Hall conductivity with field at 5 K. Despite the vanishing net magnetization, a finite anomalous Hall effect (AHE) of about 20 S/cm is observed in the high-field region, which is relatively smaller than our simulated value. It possibly arises from the intrinsic Berry curvature distribution of the Weyl points (see theoretical results). A recent report on noncollinear antiferromagnets with zero net magnetization indeed shows a large AHE which is proposed to originate from a nonvanishing Berry curvature [44–46]. There are also other theoretical studies which predicted large AHE in Weyl semimetals exhibiting a chiral anomaly [23]. In these cases, the anomalous Hall conductance (AHC) is proportional to the separation between the Weyl nodes. As such, unlike other antiferromagnets such as Mn_3X (X = Ge, Sn, Ga, Ir, Rh, and Pt) where the AHE originates from the noncollinear magnetic structure [47], the AHE in VTaNbAl possibly originates directly from the Weyl points.

V. CONCLUSION

We report a combined experimental and theoretical prediction of a class of spin gapless semiconductors in VTaNbAl. The system shows a fully compensated ferrimagnetic behavior with a unique band structure hosting rich topological nontrivial features. Unlike conventional SGS, this class of compound shows opposite spin characters in the valence and conduction band edges, making them potential candidates for spin valves and the anomalous Nernst effect. Interestingly, VTaNbAl shows a reasonably large anomalous Hall effect in spite of a a fully compensated moment, which possibly arises from the intrinsic nonvanishing Berry curvature. Due to the compensated ferrimagnetism, the time-reversal symmetry breaks, leading to the possibility of the formation of Weyl nodes. Our *ab initio* simulation confirms the presence of four pairs of Weyl nodes near the Fermi level leading to the nonzero Berry curvature, and hence a large anomalous Hall conductivity ($\sim 100\ \Omega^{-1}\,\mathrm{cm}^{-1}$). The as-prepared sample of VTaNbAl is found to crystallize in a cubic Heusler structure with an *A*2-type structure. A magnetization measurement shows a negligibly small saturation moment ($\sim 10^{-3}\mu_B$/f.u.), agreeing fairly well with our theoretical findings of fully compensated ferrimagnetism. Resistivity (ρ) shows a metallic behavior with the signature of weak localization in the low-temperature regime. The overall T variation of ρ, however, is very weak.

ACKNOWLEDGMENTS

D.R. acknowledges the Central Research Facility (CRF), Department of Physics, IIT Delhi for providing the characterization facilities. A.A. acknowledges DST SERB, India (Grant No. CRG/2019/002050) for funding to support this research.

[1] I. M. Tsidilkovski, in *Electron Spectrum of Gapless Semiconductors*, edited by K. von Klitzing, Springer Series in Solid-State Sciences Vol. 116 (Springer, New York, 1997).

[2] G. Z. Xu, E. K. Liu, Y. Du, G. J. Li, G. D. Liu, W. H. Wang, and G. H. Wu, A new spin gapless semiconductors family: Quaternary Heusler compounds, Europhys. Lett. **102**, 17007 (2013).

[3] S. Skaftouros, K. Ozdogan, E. Sasioglu, and I. Galanakis, Search for spin gapless semiconductors: The case of inverse Heusler compounds, Appl. Phys. Lett. **102**, 022402 (2013).

[4] H. Y. Jia, X. F. Dai, L. Y. Wang, R. Liu, X. T. Wang, P. P. Li, Y. T. Cui, and G. D. Liu, Ti_2MnZ (Z = Al, Ga, In) compounds: Nearly spin gapless semiconductors, AIP Adv. **4**, 047113 (2014).

[5] L. Wang and Y. Jin, A spin-gapless semiconductor of inverse Heusler Ti_2CrSi alloy: First-principles prediction, J. Magn. Magn. Mater. **385**, 55 (2015).

[6] X. L. Wang, Proposal for a New Class of Materials: Spin Gapless Semiconductors, Phys. Rev. Lett. **100**, 156404 (2008).

[7] E. V. Gomonay and V. M. Loktev, Spintronics of antiferromagnetic systems, Low Temp. Phys. **40**, 17 (2014).

[8] R. A. de Groot, Half-metallic magnetism in the 1990s, Phys. B: Condens. Matter **172**, 45 (1991).

[9] I. Galanakis and E. Şaşıoğlu, High T_C half-metallic fully-compensated ferrimagnetic Heusler compounds, Appl. Phys. Lett. **99**, 052509 (2011).

[10] I. Galanakis, K. Ozdogan, E. Sasioglu, and B. Aktas, *Ab initio* design of half-metallic fully compensated ferrimagnets: The case of Cr_2MnZ (Z = P, As, Sb and Bi), Phys. Rev. B **75**, 172405 (2007).

[11] I. Galanakis, K. Ozdogan, and E. Sasioglu, High-T_C fully compensated ferrimagnetic semiconductors as spin-filter materials: The case of CrVXAl (X = Ti, Zr, Hf) Heusler compounds, J. Phys.: Condens. Matter **26**, 086003 (2014).

[12] Y. Zhang, Z. Liu, G. Liu, and X. Ma, Half-metallic fully compensated ferrimagnetism in $C1_b$-type half Heusler compounds $Mn_2Si_{1-x}Ge_x$, J. Magn. Magn. Mater. **387**, 67 (2015).

[13] S. Wurmehl, H. C. Kandpal, G. H. Fecher, and C. Felser, Valence electron rules for prediction of half-metallic compensated-ferrimagnetic behaviour of Heusler compounds with complete spin polarization, J. Phys.: Condens. Matter **18**, 6171 (2006).

[14] Y. Venkateswara, S. Gupta, S. S. Samatham, M. R. Varma Enamullah, K. G. Suresh, and A. Alam, Competing magnetic and spin-gapless semiconducting behavior in fully compensated ferrimagnetic CrVTiAl: Theory and experiment, Phys. Rev. B **97**, 054407 (2018).

[15] X.-T. Wang, X.-F. Dai, H.-Y. Jia, L.-Y. Wang, G.-D. Liu, X.-F. Liu, W. Yuan, and Y.-T. Cui, Three-dimensional topological insulators: Case of quaternary Heusler compounds, Rare Metals **40**, 1219 (2021).

[16] C. K. Barman, C. Mondal, B. Pathak, and A. Alam, Quaternary Heusler alloy: An ideal platform to realize triple point fermions, Phys. Rev. B **99**, 045144 (2019).

[17] P. Chaudhary, K. K. Dubey, G. K. Shukla, S. Singh, S. Sadhukhan, S. Kanungo, A. K. Jena, S.-C. Lee, S. Bhattacharjee, J. Minar, and S. W. D'Souza, Role of chemical disorder in tuning the Weyl points in vanadium doped Co_2TiSn, Phys. Rev. Mater. **5**, 124201 (2021).

[18] Z. Wang, M. G. Vergniory, S. Kushwaha, M. Hirschberger, E. V. Chulkov, A. Ernst, N. P. Ong, R. J. Cava, and B. A. Bernevig, Time-Reversal-Breaking Weyl Fermions in Magnetic Heusler Alloys, Phys. Rev. Lett. **117**, 236401 (2016).

[19] Y. Venkateswara, S. S. Samatham, P. D. Babu, K. G. Suresh, and A. Alam, Coexistence of spin semimetal and Weyl semimetal behavior in FeRhCrGe, Phys. Rev. B **100**, 180404(R) (2019).

[20] G. Chang, S.-Y. Xu, H. Zheng, B. Singh, C.-H. Hsu, G. Bian, N. Alidoust, I. Belopolski, D. S. Sanchez, D. S. Sanchez, S. Zhang, H. Lin, and M. Z. Hasan, Room-temperature magnetic topological Weyl fermion and nodal line semimetal states in half-metallic Heusler Co_2TiX (X=Si, Ge, or Sn), Sci. Rep. **6**, 38839 (2016).

[21] K. Manna, Y. Sun, L. Muechler, J. Kbler, and C. Felser, Heusler, Weyl and Berry, Nat. Rev. Mater. **3**, 244 (2018).

[22] T. Kono, M. Kakoki, T. Yoshikawa, X. Wang, K. Goto, T. Muro, R. Y. Umetsu, and A. Kimura, Visualizing Half-Metallic Bulk Band Structure with Multiple Weyl Cones of the Heusler Ferromagnet, Phys. Rev. Lett. **125**, 216403 (2020).

[23] W. Shi, L. Muechler, K. Manna, Y. Zhang, K. Koepernik, R. Car, J. van den Brink, C. Felser, and Y. Sun, Prediction of a magnetic Weyl semimetal without spin-orbit coupling and strong anomalous Hall effect in the Heusler compensated ferrimagnet Ti_2MnAl, Phys. Rev. B **97**, 060406(R) (2018); C.-H. Hsu, P. C. Sreeparvathy, C. K. Barman, F.-C. Chuang, and A. Alam, Coexistence of topological nontrivial and spin-gapless semiconducting behavior in $MnPO_4$: A composite quantum compound, *ibid.* **103**, 195143 (2021).

[24] G. Kresse and D. Joubert, From ultrasoft pseudopotentials to the projector augmented-wave method, Phys. Rev. B **59**, 1758 (1999).

[25] G. Kresse and J. Furthmuller, Efficient iterative schemes for *ab initio* total-energy calculations using a plane-wave basis set, Phys. Rev. B **54**, 11169 (1996).

[26] See Supplemental Material at http://link.aps.org/supplemental/10.1103/PhysRevB.107.134434 for further auxiliary details of computation and self-consistent field (SCF) calculation of U, atom-projected band structure and density of states, spin-up and spin-down combined band structures, the effect of spin-orbit coupling, and thermomagnetic data of VTaNbAl, which includes Refs. [27–35].

[27] G. Kresse and J. Furthmller, Efficiency of *ab initio* total energy calculations for metals and semiconductors using a plane-wave basis set, Comput. Mater. Sci. **6**, 15 (1996).

[28] G. Kresse and J. Hafner, *Ab initio* molecular dynamics for liquid metals, Phys. Rev. B **47**, 558(R) (1993).

[29] J. P. Perdew, K. Burke, and M. Ernzerhof, Generalized Gradient Approximation Made Simple, Phys. Rev. Lett. **77**, 3865 (1996).

[30] N. Marzari and D. Vanderbilt, Maximally localized generalized Wannier functions for composite energy bands, Phys. Rev. B **56**, 12847 (1997).

[31] I. Souza, N. Marzari, and D. Vanderbilt, Maximally localized Wannier functions for entangled energy bands, Phys. Rev. B **65**, 035109 (2001).

[32] N. Marzari, A. A. Mostofi, J. R. Yates, I. Souza, and D. Vanderbilt, Maximally localized Wannier functions: Theory and applications, Rev. Mod. Phys. **84**, 1419 (2012).

[33] Q. Wu, S. Zhang, H.-F. Song, M. Troyer, and A. A. Soluyanov, WannierTools: An open-source software package for novel topological materials, Comput. Phys. Commun. **224**, 405 (2018).

[34] S. L. Dudarev, G. A. Botton, S. Y. Savrasov, C. J. Humphreys, and A. P. Sutton, Electron-energy-loss spectra and the structural stability of nickel oxide: An LSDA+U Study, Phys. Rev. B **57**, 1505 (1998).

[35] Q. Gao, I. Opahle, and H. Zhang, High-throughput screening for spin-gapless semiconductors in quaternary Heusler compounds, Phys. Rev. Mater. **3**, 024410 (2019).

[36] H. B. Nielsen and M. Ninomiya, A no-go theorem for regularizing chiral fermions, Phys. Lett. B **105**, 219 (1981).

[37] The anomalous Hall conductivity is calculated by integrating the Berry curvature over the entire Brillouin zone involving occupied bands, defined as follows, $\sigma_{\alpha\beta} = -\frac{e^2}{\hbar}\int_{\mathrm{BZ}}\frac{d^3k}{(2\pi)^3}\Omega_{\alpha\beta}(k)$, where $\sigma_{\alpha\beta}$ is the anomalous Hall conductivity, and $\Omega_{\alpha\beta}(k)$ is the Berry curvature.

[38] T. Graf, C. Felser, and S. S. Parkin, Simple rules for the understanding of Heusler compounds, Prog. Solid State Chem. **39**, 1 (2011).

[39] K. Özdoğan, E. Şaşıoğlu, and I. Galanakis, Slater-Pauling behavior in LiMgPdSn-type multifunctional quaternary Heusler materials: Half-metallicity, spin-gapless and magnetic semiconductors, J. Appl. Phys. **113**, 193903 (2013).

[40] D. Rani, J. Kangsabanik, K. G. Suresh, N. Patra, D. Bhattacharyya, S. N. Jha, and A. Alam, Origin of Local Atomic Order and Disorder in $Co_2Fe_{1-x}Cr_xSi$ Heusler Alloys: Theory and Experiment, Phys. Rev. Appl. **10**, 054022 (2018).

[41] P. A. Lee and T. V. Ramakrishnan, Disordered electronic systems, Rev. Mod. Phys. **57**, 287 (1985).

[42] G. M. Stephen, I. McDonald, B. Lejeune, L. H. Lewis, and D. Heiman, Synthesis of low-moment CrVTiAl: A potential room temperature spin filter, Appl. Phys. Lett. **109**, 242401 (2016).

[43] M. E. Jamer, B. A. Assaf, T. Devakul, and D. Heiman, Magnetic and transport properties of Mn_2CoAl oriented films, Appl. Phys. Lett. **103**, 142403 (2013).

[44] J. Kübler and C. Felser, Non-collinear antiferromagnets and the anomalous Hall effect, Europhys. Lett. **108**, 67001 (2014).

[45] H. Chen, Q. Niu, and A. H. MacDonald, Anomalous Hall Effect Arising from Noncollinear Antiferromagnetism, Phys. Rev. Lett. **112**, 017205 (2014).

[46] A. K. Nayak, J. E. Fischer, Y. Sun, B. Yan, J. Karel, A. C. Komarek, C. Shekhar, N. Kumar, W. Schnelle, J. Kubler, C. Felser, and S. S. P. Parkin, Large anomalous Hall effect driven by a nonvanishing Berry curvature in the noncolinear antiferromagnet Mn_3Ge, Sci. Adv. **2**, e1501870 (2016).

[47] T. Chen, T. Tomita, S. Minami, M. Fu, T. Koretsune, M. Kitatani, I. Muhammad, D. Nishio-Hamane, R. Ishii, F. Ishii, R. Arita, and S. Nakatsuji, Anomalous transport due to Weyl fermions in the chiral antiferromagnets Mn_3X, $X =$ Sn, Ge, Nat. Commun. **12**, 572 (2021).